Connexin 30 locally controls actin cytoskeleton and mechanical remodeling in motile astrocytes

Grégory Ghézali, Jérôme Ribot, Nathan Curry, Laure-elise Pillet, Flora Boutet-Porretta, Daria Mozheiko, Charles-félix Calvo, Pascal Ezan, Isabelle Perfettini, Laure Lecoin, et al.

Received: 7 June 2022 | Revised: 4 June 2024 | Accepted: 25 June 2024

DOI: 10.1002/glia.24590

GLIA

WILEY

RESEARCH ARTICLE

Connexin 30 locally controls actin cytoskeleton and mechanical remodeling in motile astrocytes

Grégory Ghézali[1,2] | Jérôme Ribot[1] | Nathan Curry[3] | Laure-Elise Pillet[1,4] | Flora Boutet-Porretta[1,2] | Daria Mozheiko[1,2] | Charles-Félix Calvo[1] | Pascal Ezan[1] | Isabelle Perfettini[5] | Laure Lecoin[1] | Sébastien Janel[6] | Jonathan Zapata[1] | Carole Escartin[7] | Sandrine Etienne-Manneville[5] | Clemens F. Kaminski[3] | Nathalie Rouach[1,3]

[1]Center for Interdisciplinary Research in Biology, Collège de France, CNRS, INSERM, Labex Memolife, Université PSL, Paris, France

[2]Doctoral School N° 158, Sorbonne Université, Paris, France

[3]Department of Chemical Engineering and Biotechnology, University of Cambridge, Cambridge, UK

[4]Doctoral School N°562, Université Paris Cité, Paris, France

[5]Institut Pasteur, Université de Paris, CNRS, Cell Polarity, Migration and Cancer Unit, Paris, France

[6]Université de Lille, CNRS, Inserm, CHU Lille, Institut Pasteur de Lille, CIIL - Center for Infection and Immunity of Lille, Lille, France

[7]Université Paris-Saclay, CEA, CNRS, MIRCen, Laboratoire des Maladies Neurodégénératives, Fontenay-aux-Roses, France

Correspondence
Nathalie Rouach, Center for Interdisciplinary Research in Biology, Collège de France, CNRS, INSERM, Labex Memolife, Université PSL, Paris, France.
Email: nathalie.rouach@college-de-france.fr

Funding information
Medical Research Council, Grant/Award Numbers: MR/K015850/1, MR/K02292X/1; Engineering and Physical Sciences Research Council, Grant/Award Numbers: EP/H018301/1, EP/L015889/1; The Wellcome Trust, Grant/Award Numbers: 089703/Z/09/Z, 3-3249/Z/16/Z; H2020 Marie Skłodowska-Curie Actions, Grant/Award Number: 722053; FP7 Ideas: European Research Council, Grant/Award Number: 683154

Abstract

During brain maturation, astrocytes establish complex morphologies unveiling intense structural plasticity. Connexin 30 (Cx30), a gap-junction channel-forming protein expressed postnatally, dynamically regulates during development astrocyte morphological properties by controlling ramification and extension of fine processes. However, the underlying mechanisms remain unexplored. Here, we found in vitro that Cx30 interacts with the actin cytoskeleton in astrocytes and inhibits its structural reorganization and dynamics during cell migration. This translates into an alteration of local physical surface properties, as assessed by correlative imaging using stimulated emission depletion (STED) super resolution imaging and atomic force microscopy (AFM). Specifically, Cx30 impaired astrocyte cell surface topology and cortical stiffness in motile astrocytes. As Cx30 alters actin organization, dynamics, and membrane physical properties, we assessed whether it controls astrocyte migration. We found that Cx30 reduced persistence and directionality of migrating astrocytes. Altogether, these data reveal Cx30 as a brake for astrocyte structural and mechanical plasticity.

Grégory Ghézali and Jérôme Ribot contributed equally to this work.

Nathan Curry and Laure-Elise Pillet contributed equally to this work.

KEYWORDS
actin, astrocyte, connexin, motility, physical surface properties

1 | INTRODUCTION

Astrocytes are dynamic brain elements, which tightly interact with neurons to process information via active signaling and regulation of extracellular homeostasis. They display highly ramified morphologies characterized by multidinous fine processes that surround synapses and regulate their functions. Astrocytic morphogenesis takes place during the first postnatal weeks and contributes to the sculpting of developing synaptic circuits (Stogsdill et al., 2017). Remarkably, the resulting complex morphologies of astrocytes are highly plastic. Their structural properties vary with the level of neuronal activity as well as in response to cerebral insults, which can remodel astroglial branching via retraction or extension of fine processes. Notably, such astroglial remodeling occurs at the level of perisynaptic processes in physiological and pathological contexts as diverse as parturition, lactation, learning, sleep deprivation, or Parkinson's disease (Bellesi et al., 2017; Bernardinelli et al., 2014; Perez-Alvarez et al., 2014; Theodosis, 2002; Villalba & Smith, 2011).

The molecular determinants of astroglial remodeling are still poorly understood. We have recently shown that Cx30, an astroglial gap-junction subunit expressed postnatally, controls the extension, ramification, and polarity of astroglial processes in the hippocampus during development (Ghezali et al., 2018; Pannasch et al., 2014). Interestingly, the Cx30-dependent morphological regulations occur at the whole-cell level as well as at perisynaptic sites. Cx30 indeed regulates both the spatial orientation of protrusions throughout the entire astrocyte territory (Ghezali et al., 2018) and their local insertion into synaptic clefts (Pannasch et al., 2014). Such regulations have functional impact, as they contribute to the polarity of gap-junction mediated astroglial networks (Ghezali et al., 2018) and to synaptic transmission (Pannasch et al., 2014). However, the molecular mechanisms underlying Cx30-mediated astroglial structural plasticity remain largely unknown.

The intracellular C-terminal tail of Cx subunits contains various protein binding motifs and thus constitutes a signaling platform for Cx-interacting proteins (Herve et al., 2007). For instance, Cx30 has been shown to interact with the cytoskeleton in tumoral (Qu et al., 2009) and cochlear cells (Defourny et al., 2019). Similarly, Cx43, the other astroglial Cx, interacts with numerous proteins, including membrane channels and receptors (Fortes et al., 2004; Giepmans et al., 2003; Yue et al., 2006), enzymes (Herve et al., 2007), cytoskeletal proteins (Olk et al., 2010), and adhesion molecules (Wei et al., 2005). Furthermore, Cx43 mediates intercellular adhesion between cortical neurons and radial glia, which is crucial for neurodevelopment (Elias et al., 2007). Cxs also play an important role in cell motility in various systems, from migration of neural progenitors (Cina et al., 2009; Fushiki et al., 2003) to glioma cell invasion (Kotini & Mayor, 2015). Furthermore, during polarized migration, we previously reported that astrocytes display a structural plasticity of the actin cytoskeleton and surface topography (Curry et al., 2017), which are known mediators of morphological changes (Fletcher & Mullins, 2010). In addition, we showed that this structural remodeling is associated with a functional plasticity of membrane stiffness, a key mechanical property for cell remodeling (Curry et al., 2017). Cx30 is a determinant of astroglial morphological plasticity (Ghezali et al., 2018; Pannasch et al., 2014), but the underlying molecular mechanisms remain unknown. We thus investigated the role of Cx30 in actin cytoskeleton organization and remodeling during migration, and its impact on astrocyte membrane functional plasticity and cellular motility. Here, we show that astroglial Cx30 interacts with the actin cytoskeleton, alters its dynamic remodeling, and modifies the mechanical and motile properties of astrocytes.

2 | MATERIALS AND METHODS

2.1 | Animals

Experiments were carried out according to the guidelines of the European Community Council Directives of January 1st 2013 (2010/63/EU) and French regulations (Code Rural R214/87-130). Experimental procedures were approved by our local ethics committee Comité d'éthique en expérimentation animal (CEEA n°059, Paris Centre et Sud) and registered with the French Research Ministry (APAFIS n° 2015071010466740 and 2019021211024807). All applicable international, national, and/or institutional guidelines for the care and use of animals were followed. Adult mice were group housed on a 12-hr light/dark cycle, with ad libitum access to food and water. All efforts were made to minimize the number of used animals and their suffering, taking into consideration the "3Rs recommendation" (replacement, reduction, and refinement) for animal experimentation. Experiments were performed in wild type mice, Swiss and IP3R2$^{-/-}$ mice (Li et al., 2005), which were provided by J. Chen, University of California San Diego (USA). Mice of both sexes were used.

2.2 | Primary astrocyte cultures

Primary cortical mouse astrocyte cultures were prepared as previously described (Koulakoff et al., 2008). Briefly, brains were removed from Swiss newborn pups (P1–P3) and the cortices were dissected in cold Phosphate-buffered saline (PBS) -glucose (33 mM). Meninges were carefully withdrawn and cortices were mechanically dissociated with flame-polished Pasteur pipette in PBS-glucose. Cells were seeded on poly-ornithine coated glass coverslips (for imaging) or Petri dishes (for biochemistry) in Dulbecco's Modified Eagle Medium (DMEM) containing 10% fetal calf serum, 10 U/mL penicillin, and 10 µg/mL streptomycin (GIBCO) and incubated at 37°C, 5% CO_2. After 1 week, once cells have reached confluency, 1 µM of cytosine-arabinoside was added to the cell culture for 3 days to eliminate proliferating microglial

cells. Medium was then changed every 3 days and cells were used after 2–3 weeks in culture.

2.3 | Lentivirus production

Self-inactivated (SIN) lentiviruses containing the central polypurine tract (cPPT) sequence, the mouse phosphoglycerate kinase I promoter (PGK), and the woodchuck post-regulatory element (WPRE) sequence were produced. The Gateway system (Invitrogen) was used to clone cDNA of green fluorescent protein (*GFP*), mouse *Cx30* from the pENTR-D-TOPO plasmid (Invitrogen) into the SIN-cPPT-PGK-Gateway-WPRE-miR124T plasmid. Viruses (lenti-GFP and lenti-Cx30) were produced in 293 T cells using a four-plasmid system as previously described (Escartin et al., 2006) and were pseudotyped with the G-protein of the vesicular stomatitis virus (Naldini et al., 1996). Lentiviruses were diluted in 0.1 M PBS with 1% bovine serum albumin (BSA) at a final concentration of 20 ng p24/μL. Cell cultures were infected at DIV20 and studied at DIV27.

2.4 | Antibodies and immunoblotting

All the antibodies used in this study are commercially available and have been validated in previous studies, as reported by the suppliers. The following primary antibodies were used: Cx30 rabbit polyclonal (1:500, 71–2200, Zymed Laboratories) and β-actin mouse monoclonal (1:10,000, A5316, Sigma). The Horseradish peroxidase (HRP) -conjugated primary anti-GAPDH antibody (1:10,000, ab9385, Abcam) was used as loading control. The following HRP-conjugated secondary antibodies were used: goat anti rabbit IgG (1:2500, sc-2004, Santa Cruz), goat anti-mouse IgG (1:2500, sc-2005, Santa Cruz).

Western blotting and quantification were performed as previously described (Pannasch et al., 2011). Shortly, cells were collected with a folded pipette tip (200 μL) in a small volume of PBS containing a cocktail of protease inhibitors (Boehringer), phosphatases inhibitors (β-glycerophosphate, 10 mM) and orthovanadate (1 mM), to which Laemmli 5X buffer was added. Samples were sonicated, boiled 5 min and loaded on 10% or 4%–12% polyacrylamide gels. Proteins were separated by electrophoresis and transferred onto nitrocellulose membranes. Membranes were saturated with 5% fat-free dried milk in triphosphate buffer solution and incubated overnight at 4°C with primary antibodies. They were then washed and exposed to peroxidase-conjugated secondary antibodies. Specific signals were revealed with the chemiluminescence detection kit (enhanced chemiluminescence (ECL), GE Healthcare (GE), Healthcare). Semi-quantitative densitometric analysis was performed after scanning the bands with the imageJ software.

2.5 | Pull-down

Astrocytes expressing Cx30 (lenti-Cx30) were washed in PBS, lysed at 4°C in lysis buffer (10 mM HEPES, 5 mM $MgCl_2$, 150 mM KCl, 1 mM dithiothreitol (DTT), 0.1% Triton) and centrifugated for 20 min at 15,000 *g* at 4°C. The supernatant was incubated with agarose beads for 30 min at 4°C under stirring to prevent unspecific binding. Cx30-expressing astrocyte lysates (input) were then incubated for 1 h at 4°C with either anti-Cx30 (IP Cx30) or anti-rabbit-IgG (IP IgG) beads. Lysates were discarded and beads were washed with lysis buffer. Agarose beads were incubated with Laemmli at 56°C for 4 min and pulled-down proteins were analyzed by Sodium Dodecyl Sulphate-Polyacrylamide Gel Electrophoresis (SDS-PAGE) followed by Western-Blotting.

2.6 | Yeast-two-hybrid

The yeast two-hybrid interaction assays were performed by Hybrigenics Services SAS, Paris, France (http://www.hybrigenics-services.com).

The coding sequence of the full-length mouse Cx30 [aa. 2-261] (GenBank accession number NM_008128.1) was Polymerase Chain Reaction (PCR) -amplified and cloned in frame with the Gal4 DNA binding domain (DBD) into plasmid pB6 (as Gal4-bait fusion). pB6 derives from the original pAS2ΔΔ vector (Fromont-Racine et al., 1997). Hybrigenics' reference for this construct is hgx519v1_pB6.

The coding sequence of the full-length mouse β-Actin [aa. 1–375] (GenBank accession number NM_007393.5) was cloned in frame with the Gal4 Activation Domain (AD) into plasmid pP7 (AD-prey), derived from the original pGADGH (Bartel et al., 1993). Hybrigenics' reference for this construct is hgx4925v1_pP7. All constructs were checked by sequencing the inserts.

Baits and preys constructs were transformed in the yeast haploid cells CG1945 (*MAT*a) and YHGX13 (Y187 *ade2-101:loxP-kanMX-loxP*, *MAT*α), respectively. The diploid yeast cells were obtained using a mating protocol with both yeast strains (Fromont-Racine et al., 1997). These assays are based on the *HIS3* reporter gene (growth assay without histidine). As negative controls, the bait plasmid was tested in the presence of empty prey vector (pP7) and the prey plasmid was tested with the empty bait vector (pB66, derives from pB6). The interaction between Suppressor of Mothers against Decapentaplegic (SMAD) and Smad ubiquitination regulatory factor (SMURF) was used as positive control (Colland et al., 2004).

Controls and interactions were tested in the form of streaks of three independent yeast clones for each control and interaction on DO-2 and DO-3 selective media. The DO-2 selective medium lacking tryptophan and leucine was used as a growth control and to verify the presence of the bait and prey plasmids. The DO-3 selective medium without tryptophan, leucine, and histidine selects for the interaction between bait and prey.

2.7 | Scratch-induced migration assay

Cultured astrocytes, which do not express Cx30 (Figure S2a–c), were transfected with lipofectamin 24 h before wounding with plasmids for GFP (Control), Cx30-venus (Beltramello et al., 2003; Ghezali et al., 2018), Cx30-GFP (pRP-eGFP-CMV *Human Cx30*, Vector Builder), Cx30T5M-GFP (pRP-eGFP-CMV *Human Cx30T5M*, Vector Builder) or C-terminally-truncated Cx30, lacking the last 28 amino acids at the

C-terminus (Cx30ΔCter-GFP) (pRP-eGFP-CMV *Human Cx30*ΔCter, Vector Builder). The medium was changed 12 h before performing scratch-induced migration assays. Confluent astrocytes were wounded by tidily scraping monolayers with a 200 µL pipette tip (≈300 µm in width) and imaged 8 h after the scratch, unless otherwise stated.

Astrocyte migration was monitored with a phase contrast microscope every 15 min after wounding during 24 h. Transfected cells were identified with a fluorescent reporter gene and analysis of migration was performed by tracking cell nuclei using the "Manual Tracking" plugin on ImageJ. Migration speed, persistence, and directionality were then calculated between 16 and 24 h of migration.

2.8 | Imaging analysis of astroglial filopodia-like protrusions

Primary astrocyte cultures were transfected with Lifeact-red fluorescent protein (RFP), a F-actin fluorescent marker, and either GFP or Cx30. Following scratch-induced migration assay, wound-edge astrocytes were imaged for 4 h with high magnification (63× objective) at a frame rate of 12 images per hour using a Leica DM IRB/E inverted video-microscope equipped for transmitted light and fluorescence live-cell imaging. Time-lapse videos of individual migrating astrocytes were then analyzed with the ImageJ plugin *FiloQuant* (Barry et al., 2015; Jacquemet et al., 2017) for the automated measurement of actin-rich filopodia-like protrusions number and size. The filopodial density was expressed as the number of filopodia per unit of surface (μm^2).

2.9 | STED microscopy

Stimulated emission depletion (STED) imaging was performed using either a home-built STED microscope designed for correlative STED/atomic force microscopy (AFM) imaging, as previously described (Curry et al., 2017) or a custom upright STED microscope for live imaging (Abberior Instruments). The latter is based on a Scientifica microscope body (Slice Scope, Scientifica) with an Olympus 100X/1.4NA ULSAPO objective lens. It comprises a scanner design featuring four mirrors (Quad Scanner, Abberior Instruments). 488 and 640 nm excitation lasers (Abberior Instruments, pulsed @40/80 Mhz) and two STED-lasers at 595 nm (MPB-C, cw) and 775 nm (MPB-C, pulsed @40/80 MHz) are available. The laser excitation and STED laser beams are superimposed using a beam-splitter (HC BS R785 lambda/10 PV flat, AHF Analysetechnik). Excitation power with pulsed excitation ranged from 10 to 20 µW with STED powers of up to 200 mW in the focal plane.

2.10 | Quantitative analysis of actin filaments properties

For non-migrating astrocytes, STED images of SiR-actin labeled cytoskeleton were analyzed with *Microfilament Analyzer* (Jacques et al., 2013) to evaluate fiber density and orientation in single astrocytes. The cells' boundaries were manually defined and the portions of filaments with at least 250 nm length were automatically detected by identifying those lying on top of an oriented grid rotating every 5°. The preferred orientation of the cell's filaments was defined as the one with the highest occurrence, and the distribution of orientations was plotted with respect to the deviation from the preferred orientation. The homogeneity of the filaments orientations was then defined as the percentage of orientations falling within 15° from the preferred orientation, and the fibers density as the number of detected filaments divided by the cell's surface.

For migrating astrocytes, actin fibers with various orientations were generally intermingled at the cells edges, making the *Microfilament Analyzer* method unusable. We thus used an analysis relying on the 2D Fourier transform of regions of interest (ROI) to estimate the local orientation of the fibers and the strength of the anisotropy (Durande et al., 2019). For each cell, a ROI was first manually defined by covering the edges of the cells. Fourier transform was then applied on 3 × 3 µm ROI windows that were separated by 500 nm. Finally, the orientation of the fibers and the strength of such anisotropy was defined as the circular averaging of all the orientation vectors contained in the ROI. With this method, the strength of the anisotropy is normalized between zero and one, a zero-value indicating that fibers are disorganized within the ROI, and a one value indicating that fibers are parallel to each other.

2.11 | Atomic force microscopy

STED and AFM coupled acquisitions were acquired on the AFM system (Bioscope RESOLVE, Bruker) directly mounted on the STED inverted optical microscope. The nanoscope software (Bruker) was used to control AFM acquisition. Acquisitions were performed using the peak force quantitative nanomechanic live cell mode (PFQNM—live cell) of the software. Probes optimized for live cell nanomechanic imaging (PFQNM-LC, Bruker) were used throughout (Schillers et al., 2016). The spring constant of each probe was pre-calibrated and the no touch calibration option of the software was used to measure the deflection sensitivity. The peak force set point was optimized by the user based on the measured force curves. Sample deformation of less than 100 nm was maintained. Cells were imaged in culture medium containing 10% HEPES buffer. The sample stage was heated to 37°C. Modulus of the sample was calculated offline using nanoscope analysis software (Bruker). Stiffness values were calculated by fitting a cone-sphere model.

Widefield and AFM acquisitions were performed using a scanning force microscope NanoWizard 4 BioAFM Company name (JPK) mounted on a Z1 Axio Observer epifluorescence microscope (Zeiss). Measurements were doned using AC40 probes (Bruker). Spring constant was determined upon calibration by the thermal noise method. Quantitative imaging (QI) (JPK, Berlin, Germany) of the protrusion leading edge was conducted. Typically, an AFM map of 10 × 10 µm corresponding to 256 × 256 pixels was acquired at an appropriate scan speed (100–200 µm/s) and the lowest setpoint possible (typically 0.2 nN) to prevent damage to the

sample. AFM image processing and analysis were Modulus of the sample was performed offline using nanoscope analysis software (Bruker) or using JPK data processing software and ImageJ. Stiffness values were calculated by fitting a cone-sphere model.

2.12 | Correlative STED/AFM

All images were taken on a correlative optical/AFM microscope. The MIROview software (Nanoscope, Bruker) was used. First the pixel size of the STED microscope and AFM system were calibrated by taking optical images of a sample at three known AFM scan positions and measuring the translation of a common feature. The same AFM calibration file was used throughout. For correlative imaging, the AFM tip was manually centered on the optical field of view. An optical image of the sample was then acquired. This image was imported into the MIROview software and AFM fields of view were selected. Features, which appear in both images (actin filaments, borders between cells, or borders between cells and glass) were used for fine alignment of the images.

STED and confocal images were deconvolved using the Richardson–Lucy algorithm (deconvolution lab program in FIJI). The STED point spread function was estimated from an average of point spread functions (PSFs) measured using 20 nm beads; the confocal PSF was simulated using the FIJI package PSF generator.

Second order flattening was applied to the AFM topography images to remove tilt and bow. Stiffness values were an average across all pixels in a field of view based upon the cone-sphere model. Where the field of view includes two cells, then averages were taken for each cell. Where the field of view includes glass, the stiffness was measured for the cell only. Stiffness values quoted were the average stiffness for all measurements in that cell.

Fibriltool (FIJI macro) was used to determine the directionality of polarized structures in images (Boudaoud et al., 2014).

2.13 | Statistics

All data are expressed as mean ± SEM. Statistical significance for within-group comparisons was determined by two-way analysis of variance (ANOVAs) (followed by Bonferroni's post-test) or Kruskal–Wallis tests (followed by Dunn's post-test), whereas unpaired *t*-test were used for between-group comparisons, unless otherwise stated. Statistical analysis was performed with GraphPad Prism, except for the Moore-Rayleigh test that was performed with Matlab.

3 | RESULTS

3.1 | Cx30 interacts with actin filaments in astrocytes

To investigate whether Cx30 interacts with actin in astrocytes, we first performed super resolution imaging of actin using SiR-actin dye in live cultured mouse astrocytes expressing Cx30 fused to the Venus fluorescent protein (Cx30), which displays proper cellular distribution and channel function (Beltramello et al., 2003; Ghezali et al., 2018). SiR-actin, a cell permeable dye with far-red absorption-emission wavelengths, is a highly specific probe for F-actin suitable for live cell imaging as it features low cytotoxicity and high photostability, and is thus optimized for STED microscopy (Lukinavicius et al., 2014).

In contrast to confocal microscopy, with STED nanoscopy we were able to resolve individual actin filaments and fine Cx30 puncta. STED imaging revealed that Cx30 puncta were deposited along actin filaments, suggesting a close association (Figure 1a). To further investigate this interaction, we performed pull down experiments from lysates of Cx30- expressing astrocytes. We found that actin was coprecipitated with Cx30, indicating that both proteins physically interact (Figure 1b). The Cx30 interaction with actin likely occurred through a molecular complex, as a direct interaction between full length Cx30 and actin was not found using the yeast two-hybrid interaction assay (Figure 1c).

3.2 | Cx30 alters actin cytoskeleton organization and surface topology of migrating astrocytes

To investigate whether Cx30 alters actin organization during dynamic processes, we performed STED imaging of the actin cytoskeleton using SiR-actin in live astrocytes expressing GFP (Control) or Cx30-Venus (Cx30) using the scratch-induced migration assay (Etienne-Manneville, 2006). Scratching of the cell monolayer induced directed migration of wound-edge control astrocytes, which extended protrusions perpendicularly to the wound (Figure 2a). In control migrating astrocytes that did not express Cx30 (Kunzelmann et al., 1999), the cell protrusions displayed an array of actin fibers aligned with the direction of migration, as previously shown (Seetharaman & Etienne-Manneville, 2020) (Figure S1a). In contrast, the protrusions of Cx30-expressing astrocytes were devoid of an organized array of individual actin fibers (Figure S1b). In addition, in control live migrating astrocytes, actin fibers revealed within cell protrusions by STED imaging strongly correlated with the cell surface topology assessed with simultaneous AFM (Figure S1a,c). AFM height maps, a powerful tool to study 3D surface geometry of living cells (Basoli et al., 2018) indeed revealed straight structures displaying similar orientation relative to actin fibers, as analyzed by Fibriltool plugin (Figure S1a,e). In fact, within the cell protrusion, the majority of the structural elements revealed by AFM corresponded to polarized actin fibers (Figure S1a). In contrast, the surface topology of Cx30-expressing astrocytes protrusions showed a weaker correlation with the underlying actin structures and displayed different orientations with regard to the wound (Figure S1b,e), indicating a reduced contribution of actin to cell topography (Figure S1b,d).

When focusing on the front edge of astrocytes protrusions, the region in which most of actin dynamics occurs (O'Neill et al., 2023), we found that actin was also strongly affected by Cx30 expression, with disorganization of actin filaments that showed less defined structure, as observed with STED imaging of SiR actin (Figure 2a,b). We

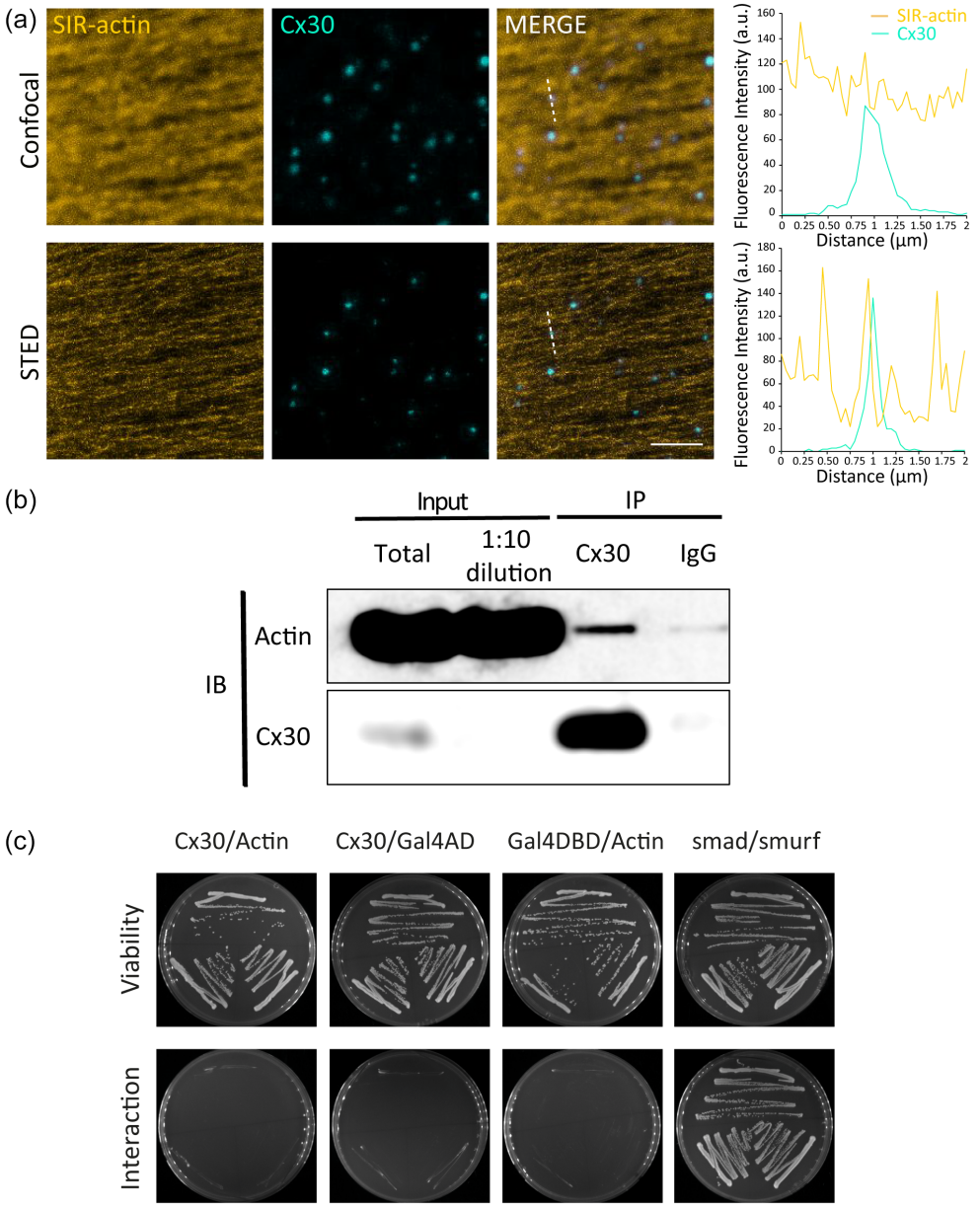

FIGURE 1 Cx30 Interacts with Actin in astrocytes. (a) Confocal and STED images of the Actin cytoskeleton labeled with the SiR-Actin dye in live astrocytes expressing Cx30-Venus. Fluorescence intensity line profiles through the indicated region (white dashed lines) reveal apposition of Cx30-Venus puncta to actin filaments in the single plane STED images. This evidence is absent in confocal images, where the resolution does not suffice to map out the actin filaments. Scale bar: 10 µM. (b) Immunoprecipitation experiments from lysates of Cx30-expressing cultured astrocytes. Bound proteins were analyzed by western blotting using an anti-Cx30 or anti-actin antibody. IB: Immunoblot; IP: Immunoprecipitation. (c) Cx30 was cloned in frame with Gal4 DNA Binding Domain (Gal4DBD, i.e. bait vector), and β-Actin in frame with Gal4 Activation Domain (Gal4AD, i.e. prey vector). Yeast cells expressing both Gal4DBD-Cx30 and Gal4AD-actin could grow on a selective medium lacking histidine, indicative of an interaction ($n = 3$). Gal4DBD and Gal4AD alone were used as negative controls ($n = 3$), while the interaction between Smad3 and Smurf1 served as positive control (Colland & Daviet, 2004). Yeast viability was checked in parallel of each interaction assay.

tested this disorganization by plotting the average orientation of actin filaments relative to the wound (Figure 2c). Circular analysis revealed that the polarization was orthogonal to the wound at the edge of protrusions in control astrocytes (Figure 2C, $n = 8$, $p < .025$, Moore-Rayleigh test), and disorganized in Cx30-expressing astrocytes (Figure 2c, $n = 13$, $p > .4$, Moore-Rayleigh test). Simultaneous AFM imaging also revealed a decreased correlation between actin fibers and the surface topography at the cell's leading edge in Cx30-expressing astrocytes (Figure 2d–f).

Remarkably, in nonmotile astrocytes, Cx30 had no significant effect on neither actin expression (Figure S2a,b), fiber density and orientation (Figure S2c,d), nor on surface topography (Figure S2e,f). Actin levels and fiber density were indeed similar in astrocytes expressing or not Cx30, as assessed by western blot (Cx30 and control: $n = 4$; Figure S2a,b) and STED microscopy (Cx30: $n = 18$; control: $n = 10$; Figure S2c,d), respectively. Further analysis with STED and AFM imaging revealed that Cx30 did not alter the orientation of actin filaments (Cx30: $n = 18$; control: $n = 10$; Figure S2c,d) and astroglial topography (Figure S2e). Altogether, these data show that Cx30 impairs actin remodeling and topology of migrating astrocytes.

3.3 | Cx30 alters stiffness of migrating astrocytes

Actin cytoskeleton not only strongly contributes to cell surface topology, but also to cell stiffness in motile astrocytes (Curry et al., 2017). We thus investigated whether the Cx30-mediated impairment of actin cytoskeleton rearrangements during migration was associated with local changes in cell stiffness. To do so, we compared surface stiffness in the center and at the front edge of the same astrocyte protrusion

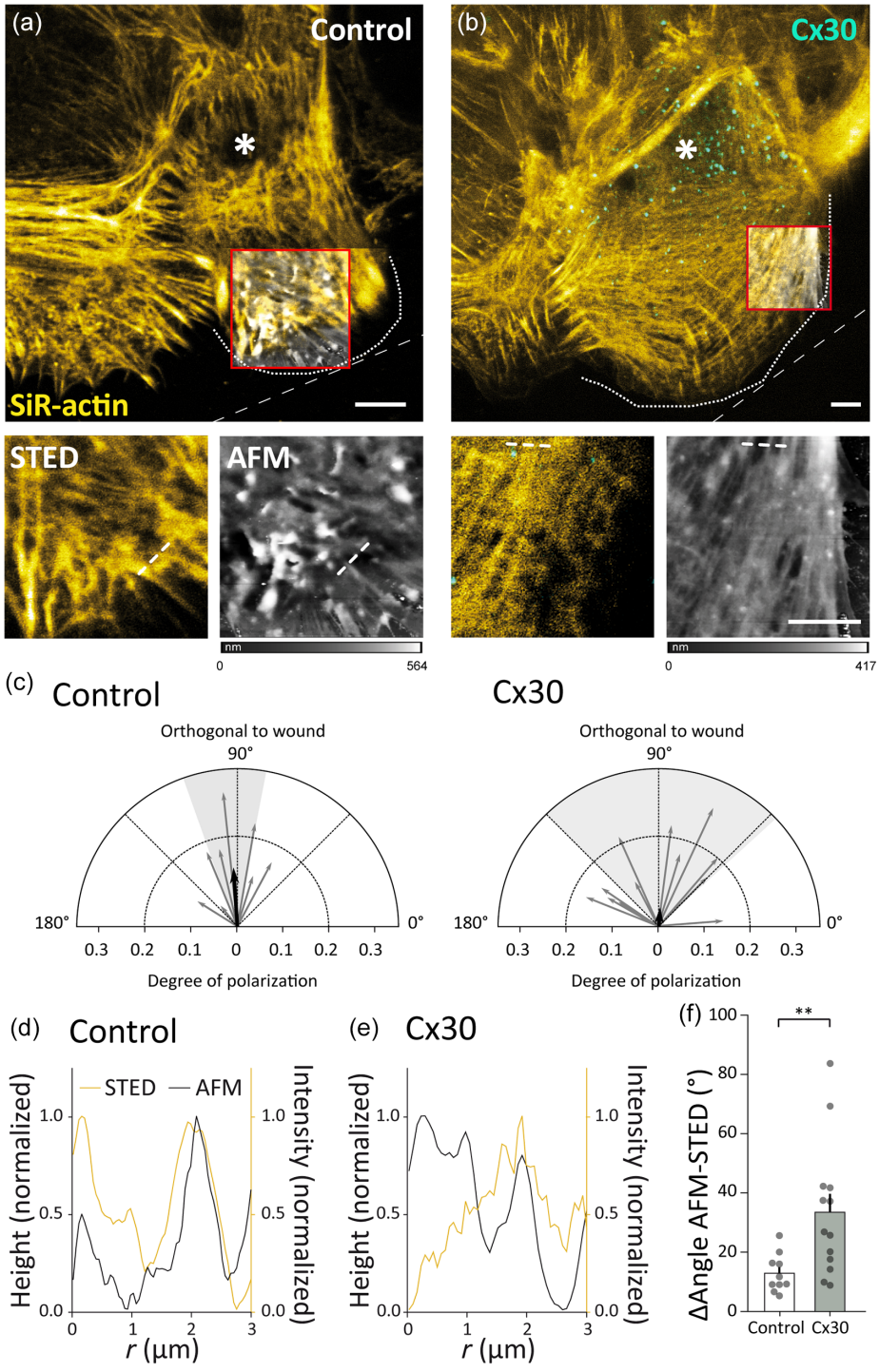

FIGURE 2 Cx30 alters actin cytoskeleton organization and surface topography at the leading edge of astrocyte protrusions during migration. (a, b) Correlative STED/AFM images of actin cytoskeleton, labeled with SiR-actin, and cell surface topography at the leading edge of control (a) and Cx30-Venus-expressing (b) astrocytes (6 h after wounding). The dotted lines and asterisks indicate the leading edges and bases of the protrusions, respectively. Zoomed STED and AFM images reveal that Cx30 profoundly disorganizes actin fibers at the protrusion's edges, and decreases their contribution to the corresponding cell surface topology. AFM color scales represent a range of heights of 0–564 nm (a) and 0–417 nm (b). Scale bars: 5 µm. (c) Polar plot of the average orientation of actin fibers at astrocytes protrusions edges. Each gray arrow represents a single astrocyte. The angle represents the average angle of fibers with respect to the wound, and the radius represents the strength of the polarization, where a zero value indicates disorganization. The circular average over the cells is shown with a black arrow and the angular variance is depicted in gray. (d, e) Line profiles through the indicated regions (white dash lines in a, b), showing the AFM (height) and STED (intensity) signals, reveal reduced correlation between the locations of peaks in Cx30-expressing astrocytes (e) compared with control (d). (f) Histogram quantifying the mean difference between the orientation relative to the wound of STED-resolved actin filaments and surface structural elements detected with AFM in control ($n = 10$) and Cx30-expressing cells ($n = 13$). Asterisks indicate statistical significance (**$p < .01$, unpaired t-test).

using AFM (Figure 3a, b). In control migrating astrocytes, stiffness was significantly higher at the leading edge (27.6 ± 3.8 kPa, $n = 11$) compared to the center of the protrusions (14.6 ± 3.4 kPa, $n = 11$, $p < 0.01$, Wilcoxon matched-pairs test, Figure 3c,e). However, Cx30 abolished this stiffness gradient as there was no apparent increase in stiffness at the leading edge (edge: 15.1 ± 3.5 vs center: 13.8 ± 2.4, $n = 9$, $p > 0.05$, Wilcoxon matched-pairs test, Figure 3d,f), which is in

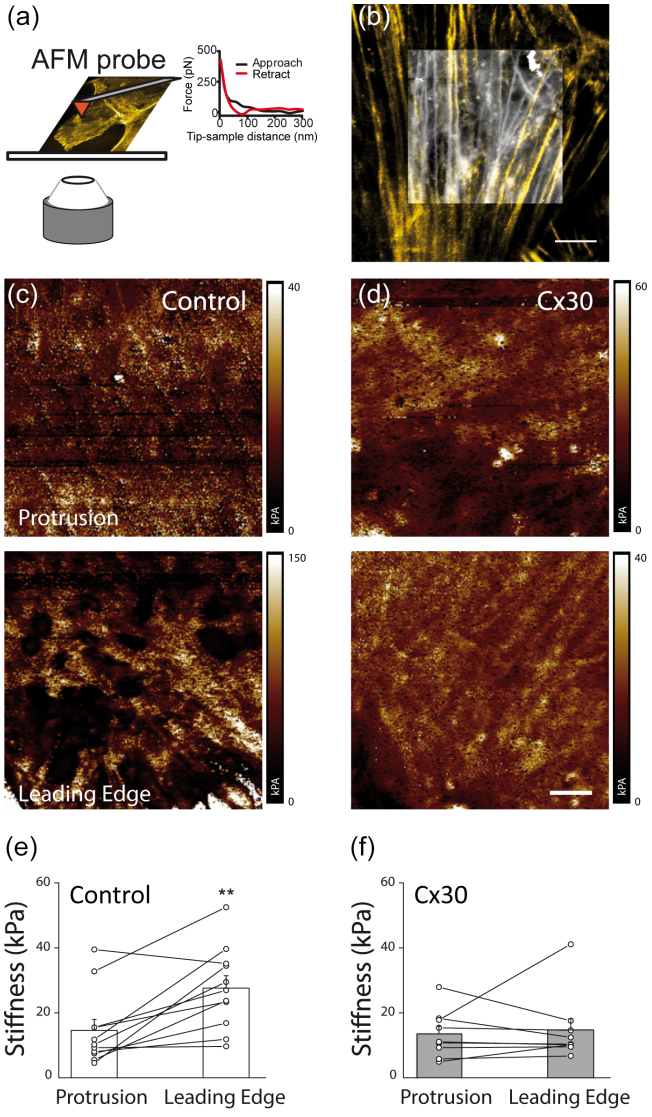

FIGURE 3 Cx30 prevents stiffness increase in astrocytes during polarized migration. (a) Schematic representation of the AFM imaging set up. AFM images (18 × 18 µm^2, 256 × 256 pixels) are taken from small regions of interest of STED images (80 × 80 µm^2). Force curves are measured for each pixel. An example of force curve is depicted, from which the modulus (stiffness) can be calculated in a given pixel. (b) Representative correlative STED/AFM image of astrocyte actin cytoskeleton (SiR-actin) and cell surface topography in a given ROI, where an average stiffness is calculated. (c, d) Maps of the membrane stiffness calculated using the cone-sphere model. Stiffness is measured within the protrusion and at the protrusion leading edge in control (c) and Cx30-expressing (d) migrating astrocytes. Scale bar: 2.5 µm. (e, f) Plots representing the distribution and mean cell stiffness of control (white, $n = 11$) and Cx30-transfected astrocytes (gray, $n = 9$), showing that Cx30 inhibits the increase of stiffness at protrusion leading edge. Asterisks indicate statistical significance (**$p < 0.01$, paired t test).

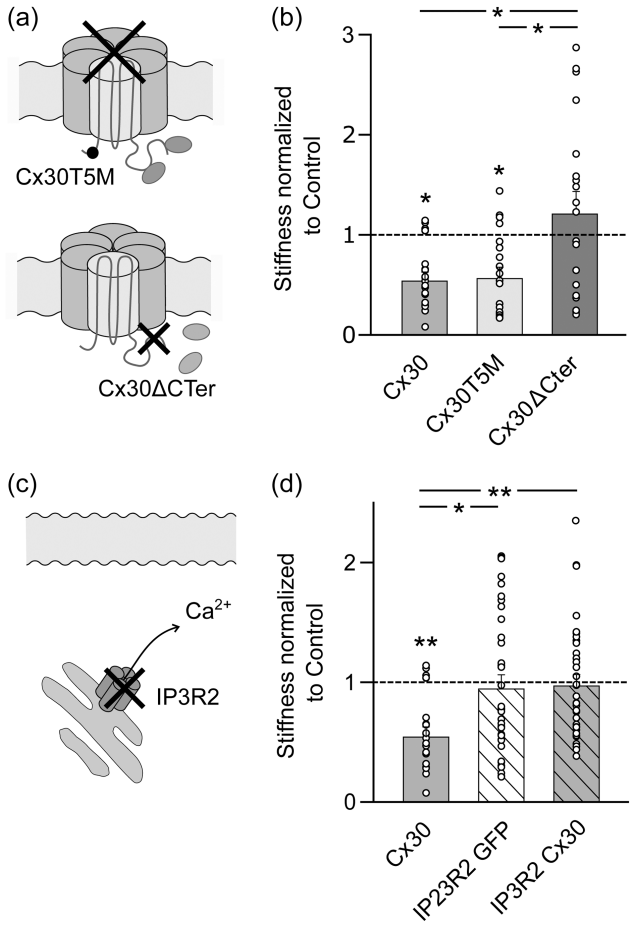

FIGURE 4 The C-terminal domain of Cx30 mediates the regulation of astrocyte stiffness via a calcium-dependent mechanism. (a) Schematic representation of Cx30 channels with the T5M point mutation, located at the N-terminal domain, leading to defective channel pore, or with a C-terminal truncation, hindering protein interactions. (b) Plots representing the distribution of stiffness in astrocytes expressing Cx30 (gray, $n = 22$), Cx30T5M (light gray, $n = 20$) or Cx30ΔC-ter (dark gray, $n = 19$) normalized to the control condition (no Cx30 expression) ($n = 33$), showing that Cx30 and Cx30T5M, but not Cx30ΔC-ter, inhibit the increase of stiffness at protrusion leading edge. Asterisks indicate statistical significance (*$p < 0.05$, Kruskall-Wallis test (KW = 16.51) followed by Dunn's post-hoc test). (c) Schematic representation of astrocytic IP3R2 channel deletion in astrocytes. IP3R2 channel is located on the membrane of the endoplasmic reticulum and its activation results in calcium release. (d) Plots representing the distribution of stiffness in astrocytes from WT mice expressing Cx30 (gray, $n = 22$), or in astrocytes from IP3R2 KO mice expressing GFP (dashed white, $n = 36$) or Cx30 (dashed gray, $n = 37$) normalized to the control condition in astrocytes from WT mice (no Cx30 expression) ($n = 33$), showing that Cx30 inhibits the increase of stiffness at protrusion leading edge via a calcium-dependent mechanism. Asterisks indicate statistical significance (*$p < 0.05$, **$p < 0.01$, Kruskall-Wallis test (KW = 14.66) followed by Dunn's post-hoc test).

agreement with the inhibitory role of Cx30 in actin rearrangement at the cell front of migrating astrocytes.

Notably, Cx30 had no significant effect on surface stiffness in nonmotile astrocytes (Control: 23.2 ± 3.3 kPa, $n = 12$; Cx30: 18.3 ± 3.1 kPa, $n = 12$, $p > 0.05$, Wilcoxon matched-pairs test, Figure S2f), which is consistent with the intact actin structure and astrocyte topology that we found in this basal condition (Figure S2c–e). Altogether, these data indicate that Cx30 locally alters astrocyte stiffness specifically during structural remodeling.

3.4 | The C-terminal domain of Cx30 regulates cortical stiffness via a calcium-dependent mechanism in migrating astrocytes

Cx30 functions involve biochemical and electrical communication via gap junctions or hemichannel, as well as channel-independent functions involving protein interactions (Mazaud et al., 2021; Theis et al., 2005). We first investigated the Cx30 function implicated in the regulation of surface stiffness at the leading edge of migrating astrocytes. To this end, we took advantage of the Cx30T5M construct, a mutated form of Cx30, in which a single point mutation, consisting in the replacement of a threonine by a methionine at position 5 of Cx30, leads to defective channel pore (Grifa et al., 1999; Schutz et al., 2010), resulting in astrocytes in inhibition of intercellular biochemical coupling, but intact membrane targeting of channels (Ghezali et al., 2018). We found that the Cx30 regulation of astrocyte stiffness at the front edge did not involve gap-junction mediated biochemical coupling as the defect in cell stiffness still occurred in astrocytes expressing the Cx30T5M construct (Figure 4a,b).

We have previously shown that Cx30 regulates astrocyte morphological plasticity via an unconventional non-channel function involving the C-terminal domain, containing binding motifs for interacting proteins (Ghezali et al., 2018; Pannasch et al., 2014). We here found that this C-terminal tail mediates the Cx30 regulation as C-terminally truncated Cx30, in contrast to full-length Cx30, had no effect on astrocyte stiffness compared to control GFP-expressing cells (Figure 4a,b).

Cell mechanical properties have been shown in various systems to be calcium-dependent (Izadi et al., 2018; Mitaku & Aruga, 1982; Qian & Xiang, 2019). We thus tested whether calcium signaling was involved in the effect of Cx30. To this end, we took advantage of the IP3R2 knockout mice, in which calcium signaling in astrocytes is strongly impaired (Li et al., 2005; Srinivasan et al., 2015). We found that calcium signaling is involved in the Cx30-mediated regulation of astrocyte stiffness, as Cx30 failed to decrease stiffness in astrocytes deficient for IP3R2 (Figure 4c,d). However, altering calcium signaling per se did not alter stiffness of control astrocytes expressing GFP (Figure 4c,d).

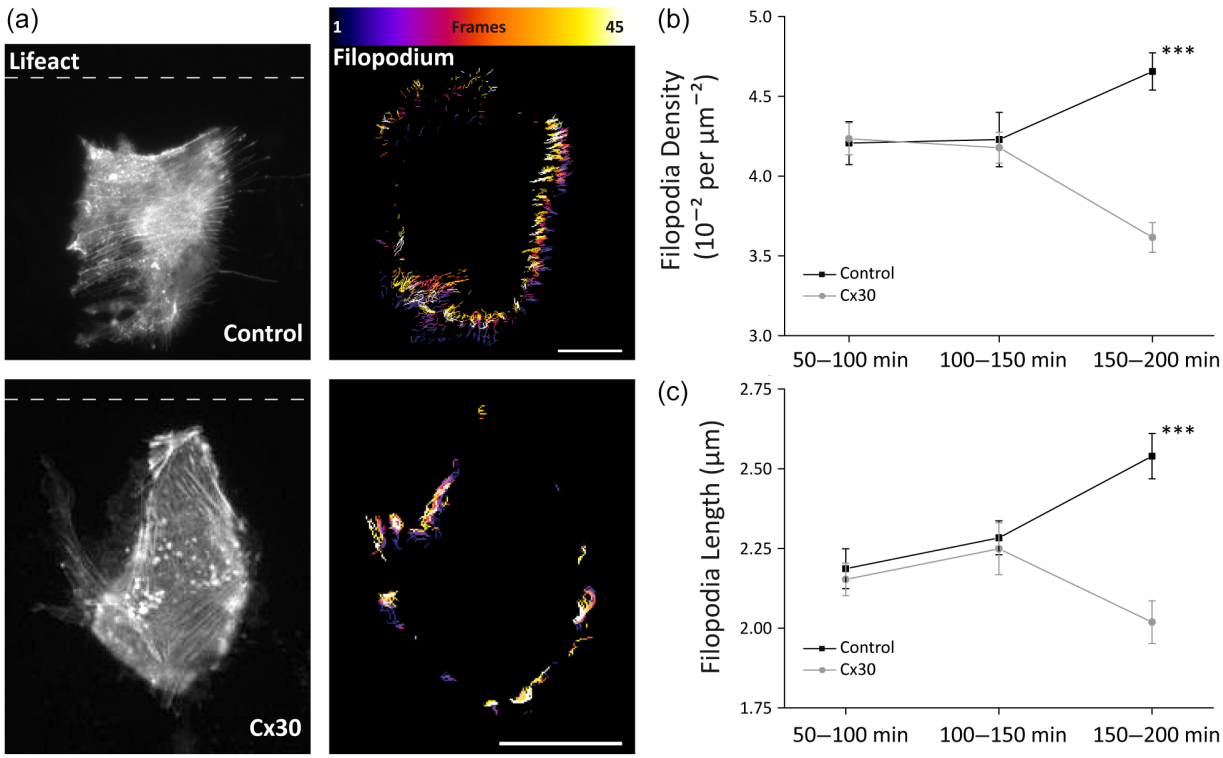

FIGURE 5 Cx30 Alters the dynamics of filopodia-like protrusions in migrating astrocytes. (a) Representative gray scale and temporal color-coded images showing GFP (Control) and Cx30-Venus (Cx30) transfected astrocytes expressing LifeAct-RFP immediately after wounding (left), and its respective actin-rich filopodium, as tracked by the FiloQuant Imagej plugin in the hours following the scratch (right). The white dashed lines indicate the position of the wound. The color scale represents the time in frames. Scale bar: 25 µm. Graph representing the time variation of the mean density (b) and length (c) of filopodia-like protrusions in Control ($n = 9$) versus Cx30 ($n = 10$) transfected astrocytes. These data show that Cx30 impairs the dynamic changes in astrocytic filopodia number and length over time. Asterisks indicate statistical significance (***$p < 0.001$).

Taken together, these results suggest that the Cx30 C-terminal domain mediates the regulation of stiffness in migrating astrocytes via a calcium-dependent mechanism.

3.5 | Cx30 alters actin-rich filopodia-like protrusions

Actin remodeling produces a driving force for membrane protrusions and cell motility (Ananthakrishnan & Ehrlicher, 2007). Since Cx30 decreases the surface stiffness at the leading edge of motile astrocytes, we investigated whether Cx30 modulates actin-rich filopodia-like protrusions in migrating astroglial cells. To do so, we performed a scratch wound assay in astrocytes expressing Lifeact-RFP, a recombinant protein, which stains specifically filamentous actin without altering its dynamic in live cells (Riedl et al., 2008) (Figure 5a). Time-lapse video microscopy combined with FiloQuant analysis (Jacquemet et al., 2017) of Lifeact-RFP-tagged cell protrusions in astrocytes transfected with Cx30-Venus showed progressive alteration in filopodia density (150–195 min: Control, 4.66 ± 0.12 $10^{-2}/\mu m^2$, $n = 10$; Cx30: 3.62 ± 0.09 $10^{-2}/\mu m^2$, $n = 10$; $p < 0.0001$, Two-way ANOVA test, Figure 5b) and length (150–195 min: Control, 2.54 ± 0.07 µm, $n = 10$; Cx30: 2.02 ± 0.07 µm, $n = 10$; $p = .0003$, Two-way ANOVA test, Figure 5c) compared to GFP-expressing (Control) cells. This indicates that Cx30 consistently alters over time properties of actin-filled filopodia in motile astrocytes.

3.6 | Cx30 regulates astroglial migration

Remodeling of actin cytoskeleton and cell mechanics is crucial for cell migration (Svitkina, 2018). Since Cx30 alters actin structure and dynamics as well as cell mechanical properties, we investigated whether Cx30 regulates astrocyte migration. To do so, we performed a scratch-induced migration assay in astrocytes expressing GFP (Control) or Cx30-Venus (Cx30). Analysis of single astrocyte trajectories during migration revealed distinct dynamic patterns (Figure 6a,b). We indeed found that Cx30 decreased both astrocyte migration persistence (16 h: $p = 0.0939$; 24 h: $p = 0.0002$, t test and Mann–Whitney, respectively) and directionality (16 h: $p = 0.0837$; 24 h: $p < 0.0001$, t test), but not velocity (16 h: $p = 0.9433$; 24 h: $p = 0.7091$, t test) (Control: $n = 27$; Cx30: $n = 20$; Figure 6). Altogether, these data indicate that Cx30 not only inhibits actin remodeling at the subcellular level, but also impairs migrating properties of whole astrocytes.

4 | DISCUSSION

Our data show that astroglial Cx30 interacts with the actin cytoskeleton. Using live cell super resolution microscopy and AFM imaging in migrating astrocytes, we found that Cx30 altered local actin remodeling as well as membrane physical properties such as cell surface topology and stiffness. Finally, Cx30 altered the properties of actin-rich protrusions and astrocyte migration. Together, these data indicate that Cx30 limits astroglial structural and mechanical plasticity during dynamic processes.

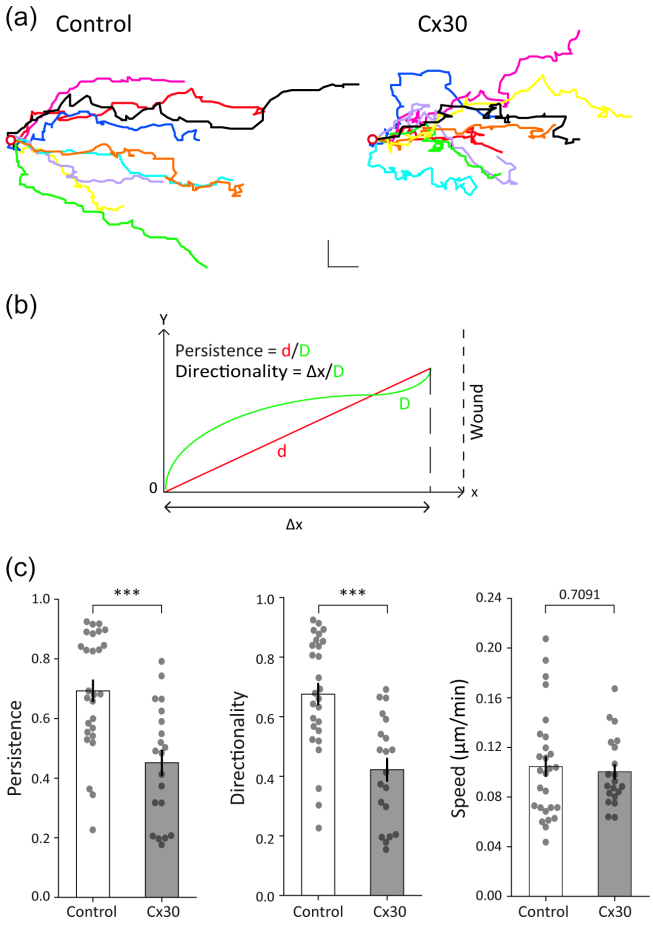

FIGURE 6 Cx30 modulates astrocyte migration.
(a) Representative trajectories of wounded astrocytes expressing GFP or Cx30-Venus (Cx30) and migrating over 24 h. Scale bars: horizontal 20 µm, vertical 20 µm. (b) Schematic representation of the method used to measure astrocyte migration directionality and persistence. (c) Quantification of migration speed, directionality and persistence in control ($n = 27$) or Cx30-expressing ($n = 20$) astrocytes between 16 and 24 h after scratching. These data show that Cx30 alters astroglial migration persistence and directionality. Asterisks indicate statistical significance (***$p < 0.001$).

4.1 | Cx30 interacts with actin and regulates its remodeling

Our data indicate that Cx30 interacts with actin in astrocytes, as found by immunoprecipitation. This interaction is likely indirect, as assessed by yeast two-hybrid assay. Cx30 and actin are thus part of a molecular complex, likely composed of cytoskeleton-associated proteins. Several Cxs have indeed been shown to interact with such adaptor proteins, including ZO-1, drebrin, cortactin or ezrin (Butkevich et al., 2004; Penes et al., 2005; Pidoux & Tasken, 2015;

Squecco et al., 2006). Ezrin is a particularly interesting partner as it is a major crosslinker of the membrane-actin interface and is enriched in fine astrocyte processes (Derouiche & Frotscher, 2001; Haseleu et al., 2013). Furthermore, it is necessary for the activity-dependent remodeling and motility of distal astrocytic processes (Lavialle et al., 2011). Alternatively, the indirect interaction between Cx30 and actin could involve Cx43, which is known to interact with numerous structural proteins such as actin in astrocytes (Olk et al., 2010) and with Cx30 in several cell types (Altevogt & Paul, 2004; Valiunas et al., 1999), although Cx43 expression levels are unchanged upon Cx30 expression in cultured astrocytes (Ghezali et al., 2018).

Notably an interaction between Cx30 and actin has been reported to support the assembly of gap junction channels in cochlear and cancer cells (Defourny et al., 2019; Qu et al., 2009). Conversely, we reveal here in live astrocytes that Cx30 controls the rearrangement and dynamics of actin filaments during migration. Remarkably, although Cx30 physically interacts with actin in basal conditions, it has no significant effect on actin level and architecture in non-motile astrocytes. This indicates that Cx30 selectively perturbs actin organization upon remodeling. Consistently, we found that Cx30 altered the properties of actin-rich filopodia and impaired whole-cell migration.

4.2 | Cx30 regulates mechanical cell properties

The actin cytoskeleton strongly contributes to cell mechanical properties during structural remodeling (Ananthakrishnan et al., 2006; Curry et al., 2017). In addition, astrocyte stiffness correlates positively with the density of cytoskeletal proteins (Gavara & Chadwick, 2016) and is modulated during development (Lee et al., 2015). Accordingly, we show here that Cx30, whose expression is developmentally regulated, impairs topography and cortical stiffness of migrating astrocytes. The Cx30 regulation of stiffness occurs independently of gap junction-mediated biochemical coupling, but may involve electrical coupling, as it is unaltered in Cx30T5M-expressing cells (Schutz et al., 2010) that we here show to display a stiffness defect. Remarkably, the effect of Cx30 on cell stiffness was mediated by its C-terminal domain, which contains binding motifs for interacting proteins (Herve et al., 2007) and occurred via a calcium-dependent mechanism in migrating astrocytes. This calcium-dependency may rely on purinergic signaling resulting from adenosine triphosphate (ATP) release via hemichannels, as Cx30T5M hemichannels are still permeable to molecules (Gaete et al., 2024). We previously reported that the C-terminal domain of Cx30 also modulates the morphological plasticity of astrocytes (Ghezali et al., 2018; Pannasch et al., 2014). This effect may thus also rely on the Cx30 interaction with actin and its role on astrocyte mechanical properties. Since we found no direct interaction between Cx30 and actin, Cx30 likely acts by regulating a molecular complex involving several cytoskeletal proteins and adhesion molecules (Defourny et al., 2019; Qu et al., 2009).

It is noteworthy that astrocyte physical properties are dysregulated in various brain diseases and likely contribute to pathogenesis. AFM experiments reveal that glioma cells show altered topographical and mechanical properties compared to normal astrocytes (Pogoda et al., 2014; Recek et al., 2015). Furthermore, changes in cell stiffness have been proposed to participate to tumor progression by inducing mechanosensitive signaling and transcription (Schrader et al., 2011), and may thus be used for diagnosis (Guck et al., 2005). Interestingly, tumorigenesis is associated with a loss in Cx30 expression, suggesting Cx30 as a tumor suppressor gene (Artesi et al., 2015; Arun et al., 2017; Princen et al., 2001). The fact that Cx30 impairs actin remodeling and migration in astrocytes suggests that loss of Cx30 in glioma promotes dynamic remodeling of the cytoskeleton and tissue invasiveness. Cx30-dependent regulation of astrocytic mechanical properties is also likely involved in neuroglial interactions. Viscoelastic measurements have shown that glial cells are very soft, softer even than neurons (Lu et al., 2006), challenging the traditional view of glial cells as rigid scaffolds for neurons. Neurons should benefit from a soft glial environment as neuronal growth has been shown in vitro to be favored on soft substrates (Flanagan et al., 2002; Georges et al., 2006; Previtera et al., 2010). In particular, the decreased stiffness found in injured reactive astrocytes might be beneficial for neuronal recovery (Miller et al., 2009). This suggests that Cx30, by promoting astroglial softness, may impact the morphological plasticity of neurons.

4.3 | Cx30 as a brake for morphological plasticity

We here report that Cx30 impairs the dynamic remodeling of actin cytoskeleton, decreases cell stiffness, and inhibits the motility of migrating astrocytes, with no effect on actin level, architecture, and membrane tension in nonmotile astrocytes. Altogether, these data point to Cx30 as a brake for morphological plasticity. This suggests that low levels of Cx30 expression, known to occur in astrocytes during early brain development (Kunzelmann et al., 1999), in response to reactivity (Koulakoff et al., 2008), or during transformation into glioma cells (Princen et al., 2001), are associated with strong structural plasticity and motility of astroglial cells. This hypothesis is consistent with the increased extension and ramification of astroglial processes deficient for Cx30 (Pannasch et al., 2014). Since astrocytes tightly interact structurally and functionally with synapses, this Cx30-dependent remodeling also likely alters the plasticity of these interactions. This may particularly be relevant during postnatal brain maturation, as the developmental increase in Cx30 expression (Kunzelmann et al., 1999) results in a reduction in astroglial coverage of hippocampal excitatory synapses (Pannasch et al., 2014), which occurs not only during maturation of the hippocampus (Lavenex et al., 2011), but also in response to neuronal activity (Perez-Alvarez et al., 2014).

AUTHOR CONTRIBUTIONS

Conception and experimental design: G.G., N.C., J.R., C.F.K., and N.R. Collection, analysis, and interpretation of the data: G.G., F. B.-P., D.M., I.P., N.C., S.J., J.R., L.E.P., C.F.C., P.E., S.E.M., C.F.K., and N.R.;

Provided reagents: L.L., J.Z., and C.E. Manuscript writing: G.G., N.C., and N.R.

ACKNOWLEDGMENTS

We thank Dr D. Mazaud for setting up STED microscopy and providing technical advice on its use in the Rouach's laboratory, Dr M. Cohen-Salmon for technical advice on molecular biology experiments, Drs. N. Déglon and A. Bemelmans for lentiviral vector production, the Orion imaging platform (IMACHEM-IBiSA) of CIRB, and especially T. Piolot and L. Martine, for assisting us with AFM recordings and analysis, M. Marchand for setting up an atomic force microscope at the College de France imaging platform and all members of the Rouach's laboratory for discussions.

This work was supported by grants from European Research Council (consolidator grant #683154), European Union's Horizon 2020 research and innovation program (Marie Sklodowska-Curie Innovative Training Networks (H2020-MSCA-ITN), grant #722053, EU-GliaPhD) and French Research Agency (ANR, Programme Blanc) to N.R., Paris Sorbonne University doctoral school ED3C and Labex Memolife to G.G., French Research Agency (ANR, Programme Blanc) to C.E., CNRS and Institut Pasteur to S.E.-M. C.F.K. acknowledges funding from the UK Engineering and Physical Sciences Research Council, EPSRC (grants EP/L015889/1 and EP/H018301/1), the Wellcome Trust (grants 3-3249/Z/16/Z and 089703/Z/09/Z) and the UK Medical Research Council, MRC (grants MR/K015850/1 and MR/K02292X/1), MedImmune, and Infinitus (China) Ltd. This project has received funding from the European Union's Horizon 2020 research and innovation programme under Grant Agreement No. 722380.

CONFLICT OF INTEREST STATEMENT

The authors declare no conflicts of interest.

DATA AVAILABILITY STATEMENT

The data that support the findings of this study are available from the corresponding author upon reasonable request.

ORCID

Sébastien Janel https://orcid.org/0000-0001-6736-3162
Carole Escartin https://orcid.org/0000-0003-3613-4118
Nathalie Rouach https://orcid.org/0000-0002-5574-888X

REFERENCES

Altevogt, B. M., & Paul, D. L. (2004). Four classes of intercellular channels between glial cells in the CNS. *The Journal of Neuroscience*, *24*(18), 4313–4323. https://doi.org/10.1523/JNEUROSCI.3303-03.2004

Ananthakrishnan, R., & Ehrlicher, A. (2007). The forces behind cell movement. *International Journal of Biological Sciences*, *3*(5), 303–317. https://doi.org/10.7150/ijbs.3.303

Ananthakrishnan, R., Guck, J., Wottawah, F., Schinkinger, S., Lincoln, B., Romeyke, M., Moon, T., & Kas, J. (2006). Quantifying the contribution of Actin networks to the elastic strength of fibroblasts. *Journal of Theoretical Biology*, *242*(2), 502–516. https://doi.org/10.1016/j.jtbi.2006.03.021

Artesi, M., Kroonen, J., Bredel, M., Nguyen-Khac, M., Deprez, M., Schoysman, L., Poulet, C., Chakravarti, A., Kim, H., Scholtens, D., Seute, T., Rogister, B., Bours, V., & Robe, P. A. (2015). Connexin 30 expression inhibits growth of human malignant gliomas but protects them against radiation therapy. *Neuro-Oncology*, *17*(3), 392–406. https://doi.org/10.1093/neuonc/nou215

Arun, S., Ravisankar, S., & Vanisree, A. J. (2017). Implication of connexin30 on the stemness of glioma: connexin30 reverses the malignant phenotype of glioma by modulating IGF-1R, CD133 and cMyc. *Journal of Neuro-Oncology*, *135*(3), 473–485. https://doi.org/10.1007/s11060-017-2608-4

Barry, D. J., Durkin, C. H., Abella, J. V., & Way, M. (2015). Open source software for quantification of cell migration, protrusions, and fluorescence intensities. *The Journal of Cell Biology*, *209*(1), 163–180. https://doi.org/10.1083/jcb.201501081

Bartel, P., Chien, C. T., Sternglanz, R., & Fields, S. (1993). Elimination of false positives that arise in using the two-hybrid system. *BioTechniques*, *14*(6), 920–924.

Basoli, F., Giannitelli, S. M., Gori, M., Mozetic, P., Bonfanti, A., Trombetta, M., & Rainer, A. (2018). Biomechanical characterization at the cell scale: Present and prospects. *Frontiers in Physiology*, *9*, 1449. https://doi.org/10.3389/fphys.2018.01449

Bellesi, M., de Vivo, L., Chini, M., Gilli, F., Tononi, G., & Cirelli, C. (2017). Sleep loss promotes astrocytic phagocytosis and microglial activation in mouse cerebral cortex. *The Journal of Neuroscience*, *37*(21), 5263–5273. https://doi.org/10.1523/JNEUROSCI.3981-16.2017

Beltramello, M., Bicego, M., Piazza, V., Ciubotaru, C. D., Mammano, F., & D'Andrea, P. (2003). Permeability and gating properties of human connexins 26 and 30 expressed in HeLa cells. *Biochemical and Biophysical Research Communications*, *305*(4), 1024–1033. https://doi.org/10.1016/s0006-291x(03)00868-4

Bernardinelli, Y., Randall, J., Janett, E., Nikonenko, I., Konig, S., Jones, E. V., Flores, C. E., Murai, K. K., Bochet, C. G., Holtmaat, A., & Muller, D. (2014). Activity-dependent structural plasticity of perisynaptic astrocytic domains promotes excitatory synapse stability. *Current Biology*, *24*(15), 1679–1688. https://doi.org/10.1016/j.cub.2014.06.025

Boudaoud, A., Burian, A., Borowska-Wykret, D., Uyttewaal, M., Wrzalik, R., Kwiatkowska, D., & Hamant, O. (2014). FibrilTool, an ImageJ plug-in to quantify fibrillar structures in raw microscopy images. *Nature Protocols*, *9*(2), 457–463. https://doi.org/10.1038/nprot.2014.024

Butkevich, E., Hulsmann, S., Wenzel, D., Shirao, T., Duden, R., & Majoul, I. (2004). Drebrin is a novel connexin-43 binding partner that links gap junctions to the submembrane cytoskeleton. *Current Biology*, *14*(8), 650–658. https://doi.org/10.1016/j.cub.2004.03.063S0960982204002374

Cina, C., Maass, K., Theis, M., Willecke, K., Bechberger, J. F., & Naus, C. C. (2009). Involvement of the cytoplasmic C-terminal domain of connexin43 in neuronal migration. *The Journal of Neuroscience*, *29*(7), 2009–2021. https://doi.org/10.1523/JNEUROSCI.5025-08.2009

Colland, F., & Daviet, L. (2004). Integrating a functional proteomic approach into the target discovery process. *Biochimie*, *86*(9–10), 625–632. https://doi.org/10.1016/j.biochi.2004.09.014

Colland, F., Jacq, X., Trouplin, V., Mougin, C., Groizeleau, C., Hamburger, A., Meil, A., Wojcik, J., Legrain, P., & Gauthier, J. M. (2004). Functional proteomics mapping of a human signaling pathway. *Genome Research*, *14*(7), 1324–1332. https://doi.org/10.1101/gr.2334104

Curry, N., Ghezali, G., Kaminski Schierle, G. S., Rouach, N., & Kaminski, C. F. (2017). Correlative STED and atomic force microscopy on live astrocytes reveals plasticity of cytoskeletal structure and membrane physical properties during polarized migration. *Frontiers in Cellular Neuroscience*, *11*, 104. https://doi.org/10.3389/fncel.2017.00104

Defourny, J., Thelen, N., & Thiry, M. (2019). Cochlear connexin 30 homomeric and heteromeric channels exhibit distinct assembly mechanisms. *Mechanisms of Development*, *155*, 8–14. https://doi.org/10.1016/j.mod.2018.10.001

Derouiche, A., & Frotscher, M. (2001). Peripheral astrocyte processes: Monitoring by selective immunostaining for the Actin-binding ERM proteins. *Glia*, *36*(3), 330–341. https://doi.org/10.1002/glia.1120

Durande, M., Tlili, S., Homan, T., Guirao, B., Graner, F., & Delanoe-Ayari, H. (2019). Fast determination of coarse-grained cell anisotropy and size in epithelial tissue images using Fourier transform. *Physical Review E*, *99*(6–1), 062401. https://doi.org/10.1103/PhysRevE.99.062401

Elias, L.A., Wang, D.D., Kriegstein, A.R. (2007). Gap junction adhesion is necessary for radial migration in the neocortex. *Nature*, *448*(7156), 901–907. https://doi.org/10.1038/nature06063. PMID: 17713529.

Escartin, C., Brouillet, E., Gubellini, P., Trioulier, Y., Jacquard, C., Smadja, C., Knott, G. W., Kerkerian-Le Goff, L., Deglon, N., Hantraye, P., & Bonvento, G. (2006). Ciliary neurotrophic factor activates astrocytes, redistributes their glutamate transporters GLAST and GLT-1 to raft microdomains, and improves glutamate handling in vivo. *The Journal of Neuroscience*, *26*(22), 5978–5989. https://doi.org/10.1523/JNEUROSCI.0302-06.2006

Etienne-Manneville, S. (2006). In vitro assay of primary astrocyte migration as a tool to study Rho GTPase function in cell polarization. *Methods in enzymology*, *406*, 565–578.

Flanagan, L. A., Ju, Y. E., Marg, B., Osterfield, M., & Janmey, P. A. (2002). Neurite branching on deformable substrates. *Neuroreport*, *13*(18), 2411–2415. https://doi.org/10.1097/01.wnr.0000048003.96487.97

Fletcher, D. A., & Mullins, R. D. (2010). Cell mechanics and the cytoskeleton. *Nature*, *463*(7280), 485–492. https://doi.org/10.1038/nature08908

Fortes, F. S., Pecora, I. L., Persechini, P. M., Hurtado, S., Costa, V., Coutinho-Silva, R., Braga, M. B., Silva-Filho, F. C., Bisaggio, R. C., De Farias, F. P., Scemes, E., De Carvalho, A. C., & Goldenberg, R. C. (2004). Modulation of intercellular communication in macrophages: Possible interactions between GAP junctions and P2 receptors. *Journal of Cell Science*, *117*(Pt 20), 4717–4726. https://doi.org/10.1242/jcs.01345jcs.01345

Fromont-Racine, M., Rain, J. C., & Legrain, P. (1997). Toward a functional analysis of the yeast genome through exhaustive two-hybrid screens. *Nature Genetics*, *16*(3), 277–282. https://doi.org/10.1038/ng0797-277

Fushiki, S., Perez Velazquez, J. L., Zhang, L., Bechberger, J. F., Carlen, P. L., & Naus, C. C. (2003). Changes in neuronal migration in neocortex of connexin43 null mutant mice. *Journal of Neuropathology and Experimental Neurology*, *62*(3), 304–314.

Gaete, P. S., Kumar, D., Fernandez, C. I., Valdez Capuccino, J. M., Liu, Y., Harris, A. L., Lup, Y. L., & Contreras, J. E. (2024). Connexin hemichannels function as molecule transporters independently of ion conduction. *Biophysical Journal*, *123*(3), 264–2265. https://doi.org/10.1016/j.bpj.2023.11.1658

Gavara, N., & Chadwick, R. S. (2016). Relationship between cell stiffness and stress fiber amount, assessed by simultaneous atomic force microscopy and live-cell fluorescence imaging. *Biomechanics and Modeling in Mechanobiology*, *15*(3), 511–523. https://doi.org/10.1007/s10237-015-0706-9

Georges, P. C., Miller, W. J., Meaney, D. F., Sawyer, E. S., & Janmey, P. A. (2006). Matrices with compliance comparable to that of brain tissue select neuronal over glial growth in mixed cortical cultures. *Biophysical Journal*, *90*(8), 3012–3018. https://doi.org/10.1529/biophysj.105.073114

Ghezali, G., Calvo, C. F., Pillet, L. E., Llense, F., Ezan, P., Pannasch, U., Bemelmans, A. P., Etienne Manneville, S., & Rouach, N. (2018). Connexin 30 controls astroglial polarization during postnatal brain development. *Development*, *145*(4). https://doi.org/10.1242/dev.155275

Giepmans, B. N., Feiken, E., Gebbink, M. F., & Moolenaar, W. H. (2003). Association of connexin43 with a receptor protein tyrosine phosphatase. *Cell Communication & Adhesion*, *10*(4–6), 201–205. https://doi.org/10.1080/cac.10.4-6.201.205

Grifa, A., Wagner, C. A., D'Ambrosio, L., Melchionda, S., Bernardi, F., Lopez-Bigas, N., Rabionet, R., Arbones, M., Monica, M. D., Estivill, X., Zelante, L., Lang, F., & Gasparini, P. (1999). Mutations in GJB6 cause nonsyndromic autosomal dominant deafness at DFNA3 locus. *Nature Genetics*, *23*(1), 16–18. https://doi.org/10.1038/12612

Guck, J., Schinkinger, S., Lincoln, B., Wottawah, F., Ebert, S., Romeyke, M., Lenz, D., Erickson, H. M., Ananthakrishnan, R., Mitchell, D., Kas, J., Ulvick, S., & Bilby, C. (2005). Optical deformability as an inherent cell marker for testing malignant transformation and metastatic competence. *Biophysical Journal*, *88*(5), 3689–3698. https://doi.org/10.1529/biophysj.104.045476

Haseleu, J., Anlauf, E., Blaess, S., Endl, E., & Derouiche, A. (2013). Studying subcellular detail in fixed astrocytes: Dissociation of morphologically intact glial cells (DIMIGs). *Frontiers in Cellular Neuroscience*, *7*, 54. https://doi.org/10.3389/fncel.2013.00054

Herve, J. C., Bourmeyster, N., Sarrouilhe, D., & Duffy, H. S. (2007). Gap junctional complexes: From partners to functions. *Progress in Biophysics and Molecular Biology*, *94*(1–2), 29–65. https://doi.org/10.1016/j.pbiomolbio.2007.03.010

Izadi, M., Hou, W., Qualmann, B., & Kessels, M. M. (2018). Direct effects of Ca(2+)/calmodulin on Actin filament formation. *Biochemical and Biophysical Research Communications*, *506*(2), 355–360. https://doi.org/10.1016/j.bbrc.2018.07.159

Jacquemet, G., Paatero, I., Carisey, A. F., Padzik, A., Orange, J. S., Hamidi, H., & Ivaska, J. (2017). FiloQuant reveals increased filopodia density during breast cancer progression. *The Journal of Cell Biology*, *216*(10), 3387–3403. https://doi.org/10.1083/jcb.201704045

Jacques, E., Buytaert, J., Wells, D. M., Lewandowski, M., Bennett, M. J., Dirckx, J., Verbelen, J. P., & Vissenberg, K. (2013). MicroFilament analyzer, an image analysis tool for quantifying fibrillar orientation, reveals changes in microtubule organization during gravitropism. *The Plant Journal*, *74*(6), 1045–1058. https://doi.org/10.1111/tpj.12174

Kotini, M., & Mayor, R. (2015). Connexins in migration during development and cancer. *Developmental Biology*, *401*(1), 143–151. https://doi.org/10.1016/j.ydbio.2014.12.023

Koulakoff, A., Ezan, P., & Giaume, C. (2008). Neurons control the expression of connexin 30 and connexin 43 in mouse cortical astrocytes. *Glia*, *56*(12), 1299–1311.

Kunzelmann, P., Schroder, W., Traub, O., Steinhauser, C., Dermietzel, R., & Willecke, K. (1999). Late onset and increasing expression of the gap junction protein connexin30 in adult murine brain and long-term cultured astrocytes. *Glia*, *25*(2), 111–119. https://doi.org/10.1002/(SICI)1098-1136(19990115)25:2<111:AID-GLIA2>3.0.CO;2-I

Lavenex, P., Sugden, S. G., Davis, R. R., Gregg, J. P., & Lavenex, P. B. (2011). Developmental regulation of gene expression and astrocytic processes may explain selective hippocampal vulnerability. *Hippocampus*, *21*(2), 142–149. https://doi.org/10.1002/hipo.20730

Lavialle, M., Aumann, G., Anlauf, E., Prols, F., Arpin, M., & Derouiche, A. (2011). Structural plasticity of perisynaptic astrocyte processes involves ezrin and metabotropic glutamate receptors. *Proceedings of the National Academy of Sciences of the United States of America*, *108*(31), 12915–12919. https://doi.org/10.1073/pnas.1100957108

Lee, S. M., Nguyen, T. H., Na, K., Cho, I. J., Woo, D. H., Oh, J. E., Lee, C. J., & Yoon, E. S. (2015). Nanomechanical measurement of astrocyte stiffness correlated with cytoskeletal maturation. *Journal of Biomedical Materials Research. Part A*, *103*(1), 365–370. https://doi.org/10.1002/jbm.a.35174

Li, X., Zima, A. V., Sheikh, F., Blatter, L. A., & Chen, J. (2005). Endothelin-1-induced arrhythmogenic Ca2+ signaling is abolished in atrial

myocytes of inositol-1,4,5-trisphosphate(IP3)-receptor type 2-deficient mice. *Circulation Research*, *96*(12), 1274–1281. https://doi.org/10.1161/01.RES.0000172556.05576.4c

Lu, Y. B., Franze, K., Seifert, G., Steinhauser, C., Kirchhoff, F., Wolburg, H., Guck, J., Janmey, P., Wei, E. Q., Kas, J., & Reichenbach, A. (2006). Viscoelastic properties of individual glial cells and neurons in the CNS. *Proceedings of the National Academy of Sciences of the United States of America*, *103*(47), 17759–17764. https://doi.org/10.1073/pnas.0606150103

Lukinavicius, G., Reymond, L., D'Este, E., Masharina, A., Gottfert, F., Ta, H., Guther, A., Fournier, M., Rizzo, S., Waldmann, H., Blaukopf, C., Sommer, C., Gerlich, D. W., Arndt, H. D., Hell, S. W., & Johnsson, K. (2014). Fluorogenic probes for live-cell imaging of the cytoskeleton. *Nature Methods*, *11*(7), 731–733. https://doi.org/10.1038/nmeth.2972

Mazaud, D., Capano, A., & Rouach, N. (2021). The many ways astroglial connexins regulate neurotransmission and behavior. *Glia*, *69*(11), 2527–2545. https://doi.org/10.1002/glia.24040

Miller, W. J., Leventhal, I., Scarsella, D., Haydon, P. G., Janmey, P., & Meaney, D. F. (2009). Mechanically induced reactive gliosis causes ATP-mediated alterations in astrocyte stiffness. *Journal of Neurotrauma*, *26*(5), 789–797. https://doi.org/10.1089/neu.2008-072710.1089/neu.2008.0727

Mitaku, S., & Aruga, S. (1982). Effect of calcium ion on the mechanical properties of lipid bilayer membrane. *Biorheology*, *19*(1/2), 185–196. https://doi.org/10.3233/bir-1982-191-221

Naldini, L., Blomer, U., Gallay, P., Ory, D., Mulligan, R., Gage, F. H., Verma, I. M., & Trono, D. (1996). In vivo gene delivery and stable transduction of nondividing cells by a lentiviral vector. *Science*, *272*(5259), 263–267.

Olk, S., Turchinovich, A., Grzendowski, M., Stuhler, K., Meyer, H. E., Zoidl, G., & Dermietzel, R. (2010). Proteomic analysis of astroglial connexin43 silencing uncovers a cytoskeletal platform involved in process formation and migration. *Glia*, *58*(4), 494–505. https://doi.org/10.1002/glia.20942

O'Neill, K. M., Saracino, E., Barile, B., Mennona, N. J., Mola, M. G., Pathak, S., Posati, T., Zamboni, R., Nicchia, G. P., Benfenati, V., & Losert, W. (2023). Decoding natural astrocyte rhythms: Dynamic Actin waves result from environmental sensing by primary rodent astrocytes. *Advanced Biology*, *7*(6), e2200269. https://doi.org/10.1002/adbi.202200269

Pannasch, U., Freche, D., Dallerac, G., Ghezali, G., Escartin, C., Ezan, P., Cohen-Salmon, M., Benchenane, K., Abudara, V., Dufour, A., Lubke, J. H., Deglon, N., Knott, G., Holcman, D., & Rouach, N. (2014). Connexin 30 sets synaptic strength by controlling astroglial synapse invasion. *Nature Neuroscience*, *17*(4), 549–558. https://doi.org/10.1038/nn.3662

Pannasch, U., Vargova, L., Reingruber, J., Ezan, P., Holcman, D., Giaume, C., Sykova, E., & Rouach, N. (2011). Astroglial networks scale synaptic activity and plasticity. *Proceedings of the National Academy of Sciences of the United States of America*, *108*(20), 8467–8472. https://doi.org/10.1073/pnas.1016650108

Penes, M. C., Li, X., & Nagy, J. I. (2005). Expression of zonula occludens-1 (ZO-1) and the transcription factor ZO-1-associated nucleic acid-binding protein (ZONAB)-MsY3 in glial cells and colocalization at oligodendrocyte and astrocyte gap junctions in mouse brain. *The European Journal of Neuroscience*, *22*(2), 404–418. https://doi.org/10.1111/j.1460-9568.2005.04225.x

Perez-Alvarez, A., Navarrete, M., Covelo, A., Martin, E. D., & Araque, A. (2014). Structural and functional plasticity of astrocyte processes and dendritic spine interactions. *The Journal of Neuroscience*, *34*(38), 12738–12744. https://doi.org/10.1523/JNEUROSCI.2401-14.2014

Pidoux, G., & Tasken, K. (2015). Anchored PKA as a gatekeeper for gap junctions. *Communicative & Integrative Biology*, *8*(4), e1057361. https://doi.org/10.1080/19420889.2015.10573611057361

Pogoda, K., Chin, L., Georges, P. C., Byfield, F. J., Bucki, R., Kim, R., Weaver, M., Wells, R. G., Marcinkiewicz, C., & Janmey, P. A. (2014). Compression stiffening of brain and its effect on mechanosensing by glioma cells. *New Journal of Physics*, *16*, 075002. https://doi.org/10.1088/1367-2630/16/7/075002

Previtera, M. L., Langhammer, C. G., Langrana, N. A., & Firestein, B. L. (2010). Regulation of dendrite arborization by substrate stiffness is mediated by glutamate receptors. *Annals of Biomedical Engineering*, *38*(12), 3733–3743. https://doi.org/10.1007/s10439-010-0112-5

Princen, F., Robe, P., Gros, D., Jarry-Guichard, T., Gielen, J., Merville, M. P., & Bours, V. (2001). Rat gap junction connexin-30 inhibits proliferation of glioma cell lines. *Carcinogenesis*, *22*(3), 507–513.

Qian, D., & Xiang, Y. (2019). Actin cytoskeleton as actor in upstream and downstream of calcium signaling in plant cells. *International Journal of Molecular Sciences*, *20*(6). https://doi.org/10.3390/ijms20061403

Qu, C., Gardner, P., & Schrijver, I. (2009). The role of the cytoskeleton in the formation of gap junctions by Connexin 30. *Experimental Cell Research*, *315*(10), 1683–1692. https://doi.org/10.1016/j.yexcr.2009.03.001

Recek, N., Cheng, X., Keidar, M., Cvelbar, U., Vesel, A., Mozetic, M., & Sherman, J. (2015). Effect of cold plasma on glial cell morphology studied by atomic force microscopy. *PLoS One*, *10*(3), e0119111. https://doi.org/10.1371/journal.pone.0119111

Riedl, J., Crevenna, A. H., Kessenbrock, K., Yu, J. H., Neukirchen, D., Bista, M., Bradke, F., Jenne, D., Holak, T. A., Werb, Z., Sixt, M., & Wedlich-Soldner, R. (2008). Lifeact: A versatile marker to visualize F-Actin. *Nature Methods*, *5*(7), 605–607. https://doi.org/10.1038/nmeth.1220

Schillers, H., Medalsy, I., Hu, S., Slade, A. L., & Shaw, J. E. (2016). PeakForce tapping resolves individual microvilli on living cells. *Journal of Molecular Recognition*, *29*(2), 95–101. https://doi.org/10.1002/jmr.2510

Schrader, J., Gordon-Walker, T. T., Aucott, R. L., van Deemter, M., Quaas, A., Walsh, S., Benten, D., Forbes, S. J., Wells, R. G., & Iredale, J. P. (2011). Matrix stiffness modulates proliferation, chemotherapeutic response, and dormancy in hepatocellular carcinoma cells. *Hepatology*, *53*(4), 1192–1205. https://doi.org/10.1002/hep.24108

Schutz, M., Scimemi, P., Majumder, P., De Siati, R. D., Crispino, G., Rodriguez, L., Bortolozzi, M., Santarelli, R., Seydel, A., Sonntag, S., Ingham, N., Steel, K. P., Willecke, K., & Mammano, F. (2010). The human deafness-associated connexin 30 T5M mutation causes mild hearing loss and reduces biochemical coupling among cochlear nonsensory cells in knock-in mice. *Human Molecular Genetics*, *19*(24), 4759–4773. https://doi.org/10.1093/hmg/ddq402

Seetharaman, S., & Etienne-Manneville, S. (2020). Cytoskeletal Crosstalk in Cell Migration. *Trends in Cell Biology*, *30*(9), 720–735. https://doi.org/10.1016/j.tcb.2020.06.004

Squecco, R., Sassoli, C., Nuti, F., Martinesi, M., Chellini, F., Nosi, D., Zecchi-Orlandini, S., Francini, F., Formigli, L., & Meacci, E. (2006). Sphingosine 1-phosphate induces myoblast differentiation through Cx43 protein expression: A role for a gap junction-dependent and -independent function. *Molecular Biology of the Cell*, *17*(11), 4896–4910. https://doi.org/10.1091/mbc.E06-03-0243

Srinivasan, R., Huang, B. S., Venugopal, S., Johnston, A. D., Chai, H., Zeng, H., Golshani, P., & Khakh, B. S. (2015). Ca(2+) signaling in astrocytes from Ip3r2(−/−) mice in brain slices and during startle responses in vivo. *Nature Neuroscience*, *18*(5), 708–717. https://doi.org/10.1038/nn.4001

Stogsdill, J. A., Ramirez, J., Liu, D., Kim, Y. H., Baldwin, K. T., Enustun, E., Ejikeme, T., Ji, R. R., & Eroglu, C. (2017). Astrocytic neuroligins control astrocyte morphogenesis and synaptogenesis. *Nature*, *551*(7679), 192–197. https://doi.org/10.1038/nature24638

Svitkina, T. (2018). The Actin cytoskeleton and Actin-based motility. *Cold Spring Harbor Perspectives in Biology*, *10*(1). https://doi.org/10.1101/cshperspect.a018267

Theis, M., Sohl, G., Eiberger, J., & Willecke, K. (2005). Emerging complexities in identity and function of glial connexins. *Trends in Neurosciences*, *28*(4), 188–195. https://doi.org/10.1016/j.tins.2005.02.006

Theodosis, D. T. (2002). Oxytocin-secreting neurons: A physiological model of morphological neuronal and glial plasticity in the adult hypothalamus. *Frontiers in Neuroendocrinology*, *23*(1), 101–135. https://doi.org/10.1006/frne.2001.0226

Valiunas, V., Manthey, D., Vogel, R., Willecke, K., & Weingart, R. (1999). Biophysical properties of mouse connexin30 gap junction channels studied in transfected human HeLa cells. *The Journal of Physiology*, *519*, 631–644. https://doi.org/10.1111/j.1469-7793.1999.0631n.x

Villalba, R. M., & Smith, Y. (2011). Neuroglial plasticity at striatal glutamatergic synapses in Parkinson's disease. *Frontiers in Systems Neuroscience*, *5*, 68. https://doi.org/10.3389/fnsys.2011.00068

Wei, C. J., Francis, R., Xu, X., & Lo, C. W. (2005). Connexin43 associated with an N-cadherin-containing multiprotein complex is required for gap junction formation in NIH3T3 cells. *The Journal of Biological Chemistry*, *280*(20), 19925–19936. https://doi.org/10.1074/jbc.M412921200

Yue, P., Zhang, Y., Du, Z., Xiao, J., Pan, Z., Wang, N., Yu, H., Ma, W., Qin, H., Wang, W. H., Lin, D. H., & Yang, B. (2006). Ischemia impairs the association between connexin 43 and M3 subtype of acetylcholine muscarinic receptor (M3-mAChR) in ventricular myocytes. *Cellular Physiology and Biochemistry*, *17*(3–4), 129–136. https://doi.org/10.1159/000092074

SUPPORTING INFORMATION

Additional supporting information can be found online in the Supporting Information section at the end of this article.

How to cite this article: Ghézali, G., Ribot, J., Curry, N., Pillet, L.-E., Boutet-Porretta, F., Mozheiko, D., Calvo, C.-F., Ezan, P., Perfettini, I., Lecoin, L., Janel, S., Zapata, J., Escartin, C., Etienne-Manneville, S., Kaminski, C. F., & Rouach, N. (2024). Connexin 30 locally controls actin cytoskeleton and mechanical remodeling in motile astrocytes. *Glia*, 1–15. https://doi.org/10.1002/glia.24590